Electronic supplementary materials

For: https://doi.org/10.1631/jzus.A2200385

Analytical solution of ground-borne vibration due to a spatially periodic harmonic moving load in a tunnel embedded in layered soil

Lihui XU[1,2], Meng MA[1,2]✉

[1]Key Laboratory of Urban Underground Engineering of Ministry of Education, Beijing Jiaotong University, Beijing 100044, China

[2]School of Civil Engineering, Beijing Jiaotong University, Beijing 100044, China

S1. Formulation of coupled periodic tunnel-soil analytical model

S1.1 Model description

Fig. S1 illustrates a tunnel embedded in a multilayered half-space in the global coordinate system. The model is periodic and comprises N+1 parts, including (N-2) standard interior soil layers where both ascending and descending waves exist, one interior layer n with a cavity where ascending, descending, and outgoing (irregular) waves exist, one semi-infinite region N where only descending waves exist, and one hollow cylinder for the tunnel where outgoing and regular waves exist. In each part, the interfaces are bonded with their adjoining parts, implying that the tractions and deflections can be directly transferred to the adjoining parts. The external force p that is periodic in space with periodicity length L and harmonic in time with circular frequency ω is applied at the bottom of the inner surface of the hollow cylinder and moves toward the positive z-axis at a constant speed of v. The material of each part is assumed to be isotropic, homogeneous, and viscoelastic; therefore, the integral transformation and superposition techniques can be applied in this case. Because the applied force is periodic in the z-direction, the entire system is periodic in the z-direction. This periodic dynamic problem can be solved by the utilisation of the generalised modal functions in the z-direction.

The geometry, local coordinate system, and state variables along the interface for each part are shown in **Fig. S2**. These parts can be further divided into four categories: standard layer, semi-infinite region, layer with a cavity, and hollow cylinder. The origin of the local coordinate system for the standard layer above the tunnel is located at its bottom interface, whereas that below the tunnel is located at its upper interface, as illustrated in **Figs. S2**a and **S2**b. The thickness of the standard layer is donated as $H_{i\ \mathrm{or}\ j}$ where $i<n$ and $j>n$. The state variable $\hat{\bar{\tilde{\mathbf{S}}}}$ is defined as the collection of the displacement vector $\hat{\bar{\tilde{\mathbf{u}}}}=[\hat{\bar{\tilde{u}}}_x,\ \hat{\bar{\tilde{u}}}_y,\ \hat{\bar{\tilde{u}}}_z]^{\mathrm{T}}$ and traction vector $\hat{\bar{\tilde{\boldsymbol{\sigma}}}}=[\hat{\bar{\tilde{\sigma}}}_{xx},\ \hat{\bar{\tilde{\sigma}}}_{xy},\ \hat{\bar{\tilde{\sigma}}}_{xz}]^{\mathrm{T}}$ as $\hat{\bar{\tilde{\mathbf{S}}}}=[\hat{\bar{\tilde{\mathbf{u}}}}^{\mathrm{T}}\ \ \hat{\bar{\tilde{\boldsymbol{\sigma}}}}^{\mathrm{T}}]^{\mathrm{T}}$ which exists at both the upper and bottom interfaces. The tilde, bar, and caret represent the Fourier transform with respect to time t, decomposition in the generalised modal space, and Fourier transform with respect to the y-coordinate, respectively. **Fig. S2**c shows the semi-infinite region, where the state variable only exists at the upper interface. **Fig. S2**d shows the layer with a cavity, where the local Cartesian and cylindrical coordinates are both located at the centre of the cavity. H_{n1} and H_{n2} denote the distances between the centre and the upper and lower interfaces, respectively. An additional state variable in terms of the cylindrical coordinate exists at the wall of the cavity, expressed as $\bar{\tilde{\mathbf{S}}}^{m}=[\bar{\tilde{\mathbf{u}}}^{m\mathrm{T}}\ \ \bar{\tilde{\boldsymbol{\sigma}}}^{m\mathrm{T}}]^{\mathrm{T}}$ where $\bar{\tilde{\mathbf{u}}}^{m}=[\bar{\tilde{u}}_{r}^{m},\ \bar{\tilde{u}}_{\varphi}^{m},\ \bar{\tilde{u}}_{z}^{m}]^{\mathrm{T}}$ and $\bar{\tilde{\boldsymbol{\sigma}}}^{m}=[\bar{\tilde{\sigma}}_{rr}^{m},\ \bar{\tilde{\sigma}}_{r\varphi}^{m},\ \bar{\tilde{\sigma}}_{rz}^{m}]^{\mathrm{T}}$. **Fig. S2**e shows the hollow cylinder for the tunnel lining with an inner radius of R and a thickness of h. The local polar coordinate system is located at the centre of the hollow cylinder, and the state variables exist at the inner and outer interfaces.

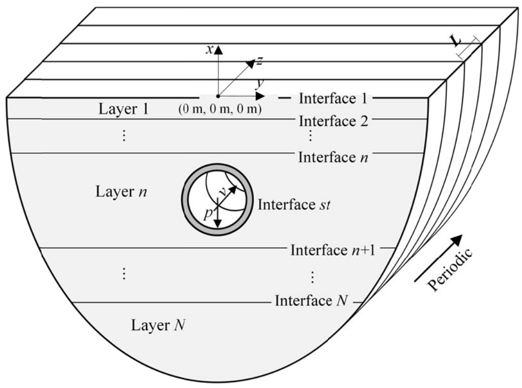

Fig. S1 Tunnel embedded in a multilayered half-space subjected to spatially periodic harmonic moving load p in a global coordinate system.

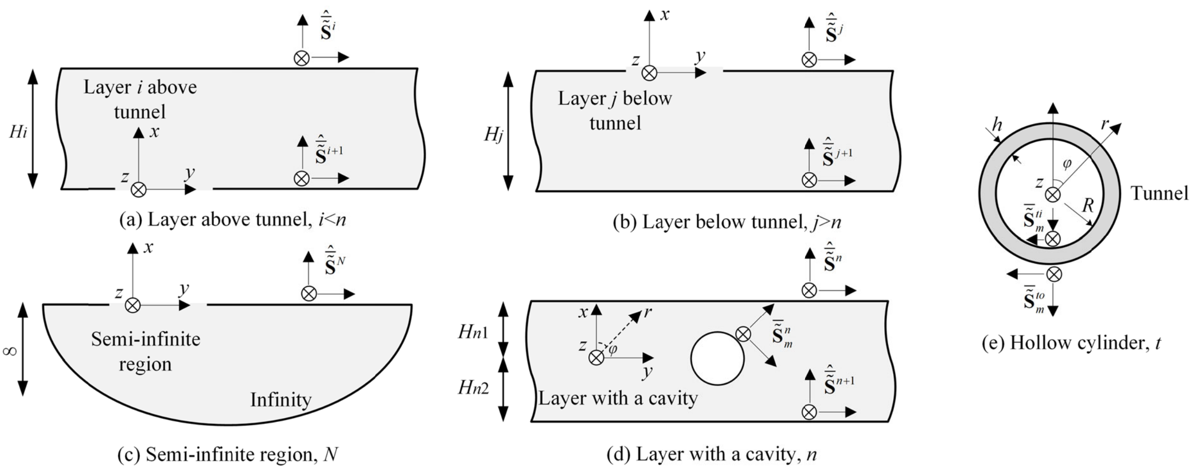

Fig. S2 The geometry, local coordinate system, and state variable at the corresponding interface of (a) and (b) soil layer above and below tunnel, (c) the semi-infinite region, (d) soil layer with a cavity, and (e) hollow cylinder for tunnel lining.

S1.2 The governing equation, Fourier transform, and generalised modal function

The motion of the isotropic, homogeneous, and viscoelastic continuum is governed by the free elastodynamics equation, expressed in vector form as (Sheng et al., 2002):

$$\mu\nabla^{2}\mathbf{u}+(\lambda+\mu)\nabla(\nabla\cdot\mathbf{u})=\rho\ddot{\mathbf{u}} \tag{S1}$$

where $\mathbf{u}$ is the displacement vector in Cartesian coordinates $\mathbf{u}=[u_x, u_y, u_z]^{\mathrm{T}}$, or in cylindrical coordinates $\mathbf{u}=[u_r, u_\varphi, u_z]^{\mathrm{T}}$. ρ is the density of the material. The symbol '¨' denotes the second-order derivative with respect to time t. λ and μ are the Lamé constants. Considering nondimensional material damping ζ, the

Lamé constants can be rewritten as $\lambda=\lambda(1+\mathrm{i}\zeta)$ and $\mu=\mu(1+\mathrm{i}\zeta)$.

To solve this equation in the frequency-wavenumber generalised modal space, the Fourier transforms with respect to time t and coordinate y are used:

$$\tilde{f}(\omega)=\int_{-\infty}^{+\infty} f(t)\mathrm{e}^{-\mathrm{i}\omega t}\mathrm{d}t, f(t)=\frac{1}{2\pi}\int_{-\infty}^{+\infty}\tilde{f}(\omega)\mathrm{e}^{\mathrm{i}\omega t}\mathrm{d}\omega \tag{S2}$$

$$\hat{f}(k_y)=\int_{-\infty}^{+\infty} f(y)\mathrm{e}^{-\mathrm{i}k_y y}\mathrm{d}y, f(y)=\frac{1}{2\pi}\int_{-\infty}^{+\infty}\hat{f}(k_y)\mathrm{e}^{\mathrm{i}k_y y}\mathrm{d}k_y \tag{S3}$$

where ω and k_y are the circular frequency and wavenumber.

As this case is a periodicity problem in the z-direction, generalised modal functions were applied in this study. Provided that the structure has a periodicity length of L under the harmonic load ω_l moving at a constant speed of v in the z-direction, the responses of adjacent points with spacing L yield the following relationship (Belotserkovskiy, 1996; Belotserkovskiy, 1998; Hussein and Hunt, 2009):

$$R(z+L,t+L/v)=\mathrm{e}^{\mathrm{i}\omega_l L/v}R\left(z,t\right) \tag{S4}$$

This is known as the periodic condition. It can be found that the response is both periodic in time and space. After applying a Fourier transform with respect to t and utilising the auxiliary periodic function of the first kind, the response in the frequency domain can be decomposed in the generalised modal space (Hussein and Hunt, 2009; Ma and Liu, 2018) as follows:

$$\tilde{R}\left(z,\omega,\omega_l\right)=\sum_{n=-\infty}^{n=+\infty}\bar{\tilde{R}}_n\left(\omega\right)\Phi_n\left(z,\omega_l,\omega\right) \tag{S5}$$

where $\Phi\left(z,\omega_l,\omega\right)$ is the generalised modal function, which takes form as follows:

$$\Phi_n\left(z,\omega_l,\omega\right)=\mathrm{e}^{\mathrm{i}\lambda_n z},\lambda_n=\frac{2\pi n}{L}+\frac{\omega_l-\omega}{v} \tag{S6}$$

With the aid of a generalised modal function, Eq. (S1) can be solved in Cartesian or cylindrical coordinates to provide the displacement and stress fields owing to the dynamic load.

S1.3 Displacement and stress solutions for each part

The governing equation of motion shown in Eq. (S1) can be solved using the techniques proposed by Schevenels (2007) and Kausel (2006). Furthermore, the expressions for displacements and stresses in both Cartesian and cylindrical coordinate systems derived in terms of the wave potential functions by Pilant (1979) can be directly applied to obtain general solutions with the aid of Eqs. (S2), (S3), and (S5).

First, the general solutions of the displacement for the standard interior layer illustrated in **Figs. S2**a and **S2**b in Cartesian coordinates can be derived as

$$\hat{\tilde{\mathbf{u}}}=[\hat{\tilde{u}}_x,\ \hat{\tilde{u}}_y,\ \hat{\tilde{u}}_z]^T=\sum_{k=1}^{3}\left(\hat{\tilde{\boldsymbol{\phi}}}_{ak}A_{ak}+\hat{\tilde{\boldsymbol{\phi}}}_{dk}A_{dk}\right) \tag{S7}$$

where vectors $\hat{\tilde{\boldsymbol{\phi}}}_{ak}$ and $\hat{\tilde{\boldsymbol{\phi}}}_{dk}$ are the ascending and descending plane wave potentials for the displacements, respectively. k=1, 2, and 3 represent P-, SH-, and SV-plane waves, respectively. A_{ak} and A_{dk} are the unknowns for ascending and descending waves, respectively. The ascending plane wave displacement potentials $\hat{\tilde{\boldsymbol{\phi}}}_{ak}$ were derived as follows (Pilant, 1979):

$$
\begin{aligned}
\hat{\tilde{\boldsymbol{\phi}}}_{a1} &= \begin{bmatrix} \mathrm{i}k_{xp} & \mathrm{i}k_y & \mathrm{i}\lambda_n \end{bmatrix}^{\mathrm{T}} \mathrm{e}^{\mathrm{i}k_{xp}x} \\
\hat{\tilde{\boldsymbol{\phi}}}_{a2} &= \begin{bmatrix} \mathrm{i}k_y & -\mathrm{i}k_{xs} & 0 \end{bmatrix}^{\mathrm{T}} \mathrm{e}^{\mathrm{i}k_{xs}x} \\
\hat{\tilde{\boldsymbol{\phi}}}_{a3} &= \begin{bmatrix} -k_{xs}\lambda_n & -k_y\lambda_n & k_{xs}^2 + k_y^2 \end{bmatrix}^{\mathrm{T}} \mathrm{e}^{\mathrm{i}k_{xs}x}
\end{aligned}
\tag{S8}
$$

where $k_{xj} = \sqrt{k_j^2 - k_y^2 - \lambda_n^2}$ (j=p *or* s) represents the wavenumbers in the x-direction. $k_j = \omega/c_j$ (j=p *or* s) are the complete wavenumbers, where the P- and S-wave velocities are expressed as $c_p = \sqrt{(\lambda + 2\mu)/\rho}$ and $c_s = \sqrt{\mu/\rho}$, respectively. To ensure that the ascending plane waves decay from the bottom interface to the upper interface, the wavenumbers in the x-direction k_{xj} (j=p *or* s) should meet the condition $\mathrm{Im}(k_{xj}) \geq 0$ (j=p *or* s).

According to the displacement-strain relationship and constitutive relationship, the traction vector can be obtained as follows by considering Eq. (S7),

$$
\hat{\tilde{\boldsymbol{\sigma}}} = [\hat{\tilde{\sigma}}_{xx},\ \hat{\tilde{\sigma}}_{xy},\ \hat{\tilde{\sigma}}_{xz}]^{\mathrm{T}} = \sum_{k=1}^{3} \left(\hat{\tilde{\boldsymbol{\varphi}}}_{ak} A_{ak} + \hat{\tilde{\boldsymbol{\varphi}}}_{dk} A_{dk} \right) \tag{S9}
$$

where $\hat{\tilde{\boldsymbol{\varphi}}}_{ak}$ and $\hat{\tilde{\boldsymbol{\varphi}}}_{dk}$ are the ascending and descending plane wave potentials for the tractions, respectively. The ascending plane traction potentials $\hat{\tilde{\boldsymbol{\varphi}}}_{ak}$ can be explicitly expressed as follows (Pilant, 1979):

$$
\begin{aligned}
\hat{\tilde{\boldsymbol{\varphi}}}_{a1} &= \mu \begin{bmatrix} 2k_p^2 - k_s^2 - 2k_{xp}^2 & -2k_{xp}k_y & -2k_{xp}\lambda_n \end{bmatrix}^{\mathrm{T}} \mathrm{e}^{\mathrm{i}k_{xp}x} \\
\hat{\tilde{\boldsymbol{\varphi}}}_{a2} &= \mu \begin{bmatrix} -2k_{xs}k_y & k_{xs}^2 - k_y^2 & -k_y\lambda_n \end{bmatrix}^{\mathrm{T}} \mathrm{e}^{\mathrm{i}k_{xs}x} \\
\hat{\tilde{\boldsymbol{\varphi}}}_{a3} &= \mu \begin{bmatrix} -2\mathrm{i}k_{xs}^2\lambda_n & -2\mathrm{i}k_{xs}k_y\lambda_n & \mathrm{i}k_{xs}\left(k_{xs}^2 + k_y^2 - \lambda_n^2\right) \end{bmatrix}^{\mathrm{T}} \mathrm{e}^{\mathrm{i}k_{xs}x}
\end{aligned}
\tag{S10}
$$

The descending plane wave potentials for displacements $\hat{\tilde{\boldsymbol{\phi}}}_{dk}$ and tractions $\hat{\tilde{\boldsymbol{\varphi}}}_{dk}$ can be obtained by directly replacing k_{xj} (j=p *or* s) with $-k_{xj}$ (j=p *or* s) in Eqs. (S8) and (S10).

Similarly, the general solutions of displacement for the hollow cylinder of the tunnel, as illustrated in **Fig. S2**e, in the cylindrical coordinate can be written as

$$
\bar{\tilde{\mathbf{u}}} = [\bar{\tilde{u}}_r,\ \bar{\tilde{u}}_\varphi,\ \bar{\tilde{u}}_z]^{\mathrm{T}} = \sum_{m=0}^{M} \sum_{k=1}^{3} \left(\bar{\tilde{\boldsymbol{\chi}}}_{ok}^m B_{ok}^m + \bar{\tilde{\boldsymbol{\chi}}}_{rk}^m B_{rk}^m \right) \tag{S11}
$$

where $\bar{\tilde{\boldsymbol{\chi}}}_{ok}^m$ and $\bar{\tilde{\boldsymbol{\chi}}}_{rk}^m$ denote the m-th order outgoing and regular cylindrical wave potentials for displacements, respectively. k=1, 2, and 3 represent the P-, SH-, and SV-waves in the cylindrical coordinate system, respectively. This series converges rapidly with respect to m, implying that using M terms in the calculation can produce satisfactory results. B_{ok}^m and B_{rk}^m are the unknown coefficients for the outgoing and regular waves, respectively. $\bar{\tilde{\boldsymbol{\chi}}}_{ok}^m$ has the following explicit expressions (Pilant, 1979):

$$
\begin{aligned}
\bar{\tilde{\boldsymbol{\chi}}}_{o1}^{m} &= \left[k_{rp} H_m^{(1)\prime}(k_{rp} r)\cos m\varphi \quad -\frac{m}{r} H_m^{(1)}(k_{rp} r)\sin m\varphi \quad \mathrm{i}\lambda_n H_m^{(1)}(k_{rp} r)\cos m\varphi \right]^{\mathrm{T}} \\
\bar{\tilde{\boldsymbol{\chi}}}_{o2}^{m} &= \left[\frac{m}{r} H_m^{(1)}(k_{rs} r)\cos m\varphi \quad -k_{rs} H_m^{(1)\prime}(k_{rs} r)\sin m\varphi \quad 0 \right]^{\mathrm{T}} \\
\bar{\tilde{\boldsymbol{\chi}}}_{o3}^{m} &= \left[\mathrm{i}k_{rs}\lambda_n H_m^{(1)\prime}(k_{rs} r)\cos m\varphi \quad -\mathrm{i}\lambda_n \frac{m}{r} H_m^{(1)}(k_{rs} r)\sin m\varphi \quad k_{rs}^2 H_m^{(1)}(k_{rs} r)\cos m\varphi \right]^{\mathrm{T}}
\end{aligned}
\tag{S12}
$$

where $k_{rj}=\sqrt{k_j^2-\lambda_n^2}$ (j=p *or* s) represents the wavenumbers in the r-direction. Similarly, the wavenumbers in the r-direction k_{rj} (j=p *or* s) should satisfy the condition $\mathrm{Im}(k_{rj})\geq 0$ (j=p *or* s). $H_m^{(1)}(\bullet)$ is the Hankel function of the first kind. The superscript prime represents the derivative with respect to $k_{rj}r$ (j=p *or* s).

Furthermore, considering the displacement–strain and constitutive relationships, the corresponding traction vector can be calculated as follows:

$$
\bar{\tilde{\boldsymbol{\sigma}}} = [\bar{\tilde{\sigma}}_{rr},\ \bar{\tilde{\sigma}}_{r\varphi},\ \bar{\tilde{\sigma}}_{rz}]^{\mathrm{T}} = \sum_{m=0}^{M}\sum_{k=1}^{3}\left(\bar{\tilde{\boldsymbol{\eta}}}_{ok}^{m} B_{ok}^{m} + \bar{\tilde{\boldsymbol{\eta}}}_{rk}^{m} B_{rk}^{m} \right)
\tag{S13}
$$

where $\bar{\tilde{\boldsymbol{\eta}}}_{ok}^{m}$ and $\bar{\tilde{\boldsymbol{\eta}}}_{rk}^{m}$ are the m-th order outgoing and regular cylindrical wave potentials for tractions, respectively. The outgoing cylindrical wave displacement potentials have the following forms (Pilant, 1979):

$$
\begin{aligned}
\bar{\tilde{\boldsymbol{\eta}}}_{o1}^{m} &= \mu\left\{ \left[(2k_p^2-k_s^2)H_m^{(1)}(k_{rp} r) + 2k_{rp}^2 H_m^{(1)\prime\prime}(k_{rp} r) \right]\cos m\varphi \quad \frac{2m}{r^2}\left[H_m^{(1)}(k_{rp} r) - k_{rp} r H_m^{(1)\prime}(k_{rp} r) \right]\sin m\varphi \quad 2\mathrm{i}\lambda_n k_{rp} H_m^{(1)\prime}(k_{rp} r)\cos m\varphi \right\}^{\mathrm{T}} \\
\bar{\tilde{\boldsymbol{\eta}}}_{o2}^{m} &= \mu\left\{ \frac{2m}{r^2}\left[k_{rs} r H_m^{(1)\prime}(k_{rs} r) - H_m^{(1)}(k_{rs} r) \right]\cos m\varphi \quad -k_{rs}^2\left[2H_m^{(1)\prime\prime}(k_{rs} r) + H_m^{(1)}(k_{rs} r) \right]\sin m\varphi \quad \frac{\mathrm{i}\lambda_n m}{r} H_m^{(1)}(k_{rs} r)\cos m\varphi \right\}^{\mathrm{T}} \\
\bar{\tilde{\boldsymbol{\eta}}}_{o3}^{m} &= \mu\left\{ 2\mathrm{i}\lambda_n k_{rs}^2 H_m^{(1)\prime\prime}(k_{rs} r)\cos m\varphi \quad \frac{2\mathrm{i}\lambda_n m}{r^2}\left[H_m^{(1)}(k_{rs} r) - k_{rs} r H_m^{(1)\prime}(k_{rs} r) \right]\sin m\varphi \quad k_{rs}(k_{rs}^2-\lambda_n^2) H_m^{(1)\prime}(k_{rs} r)\cos m\varphi \right\}^{\mathrm{T}}
\end{aligned}
\tag{S14}
$$

The regular cylindrical wave potentials for displacement $\bar{\tilde{\boldsymbol{\chi}}}_{rk}^{m}$ and traction $\bar{\tilde{\boldsymbol{\eta}}}_{rk}^{m}$ can be derived by directly replacing the Hankel function of the first kind $H_m^{(1)}(\bullet)$ with the Bessel function of the first kind $J_m^{(1)}(\bullet)$ in Eqs. (S12) and (S14), respectively.

In the semi-infinite region, as illustrated in **Fig. S2**c, only descending waves exist such that A_{ak}=0. Therefore, the displacement and traction vectors for the semi-infinite region are reduced to the following formulations from Eqs. (S7) and (S9) as follows:

$$
\hat{\hat{\tilde{\mathbf{u}}}} = [\hat{\hat{\tilde{u}}}_x,\ \hat{\hat{\tilde{u}}}_y,\ \hat{\hat{\tilde{u}}}_z]^{T} = \sum_{k=1}^{3} \hat{\hat{\tilde{\boldsymbol{\phi}}}}_{dk} A_{dk}
\tag{S15}
$$

$$
\hat{\hat{\tilde{\boldsymbol{\sigma}}}} = [\hat{\hat{\tilde{\sigma}}}_{xx},\ \hat{\hat{\tilde{\sigma}}}_{xy},\ \hat{\hat{\tilde{\sigma}}}_{xz}]^{\mathrm{T}} = \sum_{k=1}^{3} \hat{\hat{\tilde{\boldsymbol{\varphi}}}}_{dk} A_{dk}
\tag{S16}
$$

As shown in **Fig. S2**d, in the soil layer with a cavity where the tunnel is embedded, ascending, descending, and outgoing waves exist. Therefore, the displacement and traction vectors for the soil layer with a cavity in the frequency-wavenumber (ω-λ_n) domain can be expressed as:

$$
\bar{\tilde{\mathbf{u}}} = \frac{1}{2\pi}\int_{-\infty}^{+\infty}\sum_{k=1}^{3}\left(\hat{\hat{\tilde{\boldsymbol{\phi}}}}_{ak} A_{ak} + \hat{\hat{\tilde{\boldsymbol{\phi}}}}_{dk} A_{dk} \right) \mathrm{e}^{\mathrm{i}k_y y}\,\mathrm{d}k_y + \sum_{m=0}^{M}\sum_{k=1}^{3} \bar{\tilde{\boldsymbol{\chi}}}_{ok}^{m} B_{ok}^{m}
\tag{S17}
$$

$$
\bar{\tilde{\boldsymbol{\sigma}}} = \frac{1}{2\pi}\int_{-\infty}^{+\infty}\sum_{k=1}^{3}\left(\hat{\tilde{\boldsymbol{\varphi}}}_{ak} A_{ak} + \hat{\tilde{\boldsymbol{\varphi}}}_{dk} A_{dk} \right) \mathrm{e}^{\mathrm{i}k_y y}\,\mathrm{d}k_y + \sum_{m=0}^{M}\sum_{k=1}^{3} \bar{\tilde{\boldsymbol{\eta}}}_{ok}^{m} B_{ok}^{m}
\tag{S18}
$$

The above formulations show the general solutions of the displacements and tractions for the four categories stated in **Subsection 1.1**, where the boundary conditions have not yet been considered. The unknown coefficients were determined from the boundary conditions in the following derivations.

S1.4 Interactions between standard soil layers and semi-infinite region

Commonly used techniques to analytically model layered media are the transfer matrix method proposed by Thomson (1950) and Haskell (1953) and the dynamic stiffness matrix method used by Kausel (2006) and Schevenels (2007). These techniques have been successfully used in multilayered half-spaces (He et al., 2017) or tunnels embedded in half-spaces (He et al., 2018). As transformations between plane waves and cylindrical waves were performed in this study, the transfer matrix method was adopted to analytically solve the multilayered half-space, which was also applied by He et al. (2018). The coupled tunnel-soil system is considered homogeneous in the loading direction in the study by He et al. (2018), whereas it is periodic in the current study.

For the standard interior soil layer, as shown in **Figs. S2**a and **S2**b, the state variable $\hat{\tilde{\mathbf{S}}}^{l}$ (l=i or j) written in matrix form according to Eqs. (S7) and (S9) yields:

$$\hat{\tilde{\mathbf{S}}}^{l}(x^{l})=[\hat{\tilde{\mathbf{u}}}^{\mathrm{T}}\ \ \hat{\tilde{\boldsymbol{\sigma}}}^{\mathrm{T}}]^{\mathrm{T}}=\begin{bmatrix}\hat{\tilde{\boldsymbol{\phi}}}_{a}(x^{l}) & \hat{\tilde{\boldsymbol{\phi}}}_{d}(x^{l})\\ \hat{\tilde{\boldsymbol{\varphi}}}_{a}(x^{l}) & \hat{\tilde{\boldsymbol{\varphi}}}_{d}(x^{l})\end{bmatrix}\begin{bmatrix}\mathbf{A}_{a}^{l}\\ \mathbf{A}_{d}^{l}\end{bmatrix}=\mathbf{M}\left(x^{l}\right)\mathbf{A}^{l} \tag{S19}$$

where the superscript l denotes the l-th layer (l=i or j). x^{l} is the x-coordinate in the local coordinate system, as shown in **Fig. S2**. $\hat{\tilde{\boldsymbol{\phi}}}_{a}(x^{l})=\begin{bmatrix}\hat{\tilde{\boldsymbol{\phi}}}_{a1}(x^{l}) & \hat{\tilde{\boldsymbol{\phi}}}_{a2}(x^{l}) & \hat{\tilde{\boldsymbol{\phi}}}_{a3}(x^{l})\end{bmatrix}$. The other matrices have similar matrix forms. $\mathbf{A}_{a}^{l}$ and $\mathbf{A}_{d}^{l}$ are the ascending and descending wave coefficient vectors for the l-th soil layer, respectively, $\mathbf{A}_{a}^{l}$=$[\mathbf{A}_{a1}^{l}\ \mathbf{A}_{a2}^{l}\ \mathbf{A}_{a3}^{l}]^{\mathrm{T}}$ and $\mathbf{A}_{d}^{l}$=$[\mathbf{A}_{d1}^{l}\ \mathbf{A}_{d2}^{l}\ \mathbf{A}_{d3}^{l}]^{\mathrm{T}}$.

To determine the unknown coefficients, the boundary and continuous conditions between each part should be considered. Because the upper interface of the first layer (i=1) is a free surface, the tractions along this interface should satisfy the following relationship:

$$\hat{\tilde{\boldsymbol{\sigma}}}^{\mathrm{T}}\left(x^{1}=H_{1}\right)=\mathbf{0} \tag{S20}$$

Substituting Eq. (S19) into Eq. (S20), the following relationship is obtained:

$$\mathbf{A}_{a}^{1}=-\hat{\tilde{\boldsymbol{\varphi}}}_{a}^{-1}(x^{1}=H_{1})\hat{\tilde{\boldsymbol{\varphi}}}_{d}(x^{1}=H_{1})\mathbf{A}_{d}^{1}=\mathbf{R}_{ad}^{1}\mathbf{A}_{d}^{1} \tag{S21}$$

According to the compatibility and equilibrium conditions, the state variables of the standard interior layers and semi-infinite region should satisfy the following relationships because no external loads are applied at these interfaces:

$$\hat{\tilde{\mathbf{S}}}^{i-1}(x^{i-1}=0)=\hat{\tilde{\mathbf{S}}}^{i}(x^{i}=H_{i}),\ i<n \tag{S22}$$

$$\hat{\tilde{\mathbf{S}}}^{j}(x^{j}=-H_{j})=\hat{\tilde{\mathbf{S}}}^{j+1}(x^{j+1}=0),\ j>n \tag{S23}$$

The local coordinate system of the layer above the tunnel differed from that below the tunnel. Substituting Eq. (S19) into Eq. (S22) and considering each value of i=2, 3, ···, n-1, the relationship between coefficients $\mathbf{A}^{1}$ and $\mathbf{A}^{n-1}$ can be derived as follows:

$$\mathbf{A}^{1}=\mathbf{T}_{(1,n-1)}\mathbf{A}^{n-1} \tag{S24}$$

where the transfer matrix $\mathbf{T}_{(1,n\text{-}1)}$ is expressed as,

$$\mathbf{T}_{(1,n-1)}=\left\{\mathbf{M}^{-1}\left(x^{1}=0\right)\mathbf{M}\left(x^{2}=H_{2}\right)\right\}\left\{\mathbf{M}^{-1}\left(x^{2}=0\right)\mathbf{M}\left(x^{3}=H_{3}\right)\right\}\left\{\cdots\right\}\left\{\mathbf{M}^{-1}\left(x^{n-2}=0\right)\mathbf{M}\left(x^{n-1}=H_{n-1}\right)\right\} \tag{S25}$$

For a semi-infinite region, the unknown coefficients should satisfy $\mathbf{A}_a^N=\mathbf{0}$. Similarly, by substituting Eq. (S19) into Eq. (S23) and considering each value of $j=n+1$, $n+2$, ⋯, N, the relationship between the coefficients $\mathbf{A}^N$ and $\mathbf{A}^{n+1}$ can be derived as follows:

$$\mathbf{A}^N = \mathbf{T}_{(N,n+1)}\mathbf{A}^{n+1} \tag{S26}$$

where the transfer matrix $\mathbf{T}_{(N,n+1)}$ has the expression,

$$\mathbf{T}_{(N,n+1)} = \left\{\mathbf{M}^{-1}\left(x^N=0\right)\mathbf{M}\left(x^{N-1}=-H_{N-1}\right)\right\}\left\{\mathbf{M}^{-1}\left(x^{N-1}=0\right)\mathbf{M}\left(x^{N-2}=-H_{N-2}\right)\right\}\{\cdots\}\left\{\mathbf{M}^{-1}\left(x^{n+2}=0\right)\mathbf{M}\left(x^{n+1}=-H_{n+1}\right)\right\} \tag{S27}$$

Based on Eqs. (S21), (S24), and (S26), and $\mathbf{A}_a^N=\mathbf{0}$ for the semi-infinite region, the responses of the multilayered half-space under the spatially periodic harmonic moving load can be solved completely if there is no tunnel structure. Additional derivations should be performed to consider the effects of the tunnel structure.

S1.5 Interaction between standard interior layers and layer with a cavity

Three types of waves exist in the soil layer with a cavity: the ascending plane, descending plane, and outgoing cylindrical waves. To analytically model the coupled tunnel-soil system, transformations between plane and cylindrical waves should be performed, as summarised by Boström (1991). These transformation properties were successfully adopted by Yuan et al. (2017) and He et al. (2018) in a tunnel embedded in a half-space and multilayered half-space, respectively, where these models are homogeneous in the longitudinal direction.

To couple the standard layer and the layer with a cavity, the outgoing cylindrical wave should be converted into ascending or descending plane waves. These transformation properties were proposed by Boström (1991), and the transformations between wave potentials can be written as

$$\begin{aligned}
\bar{\tilde{\chi}}_{oj}^m &= \frac{1}{\pi}\int_{-\infty}^{+\infty} \frac{\hat{\tilde{\bar{\phi}}}_{aj}\mathrm{e}^{\mathrm{i}k_y y}}{k_{xj}} T_{mj}^- \mathrm{d}k_y \\
\bar{\tilde{\chi}}_{oj}^m &= \frac{1}{\pi}\int_{-\infty}^{+\infty} \frac{\hat{\tilde{\bar{\phi}}}_{dj}\mathrm{e}^{\mathrm{i}k_y y}}{k_{xj}} T_{mj}^+ \mathrm{d}k_y
\end{aligned} \tag{S28}$$

where the cylindrical waves are converted into ascending and descending plane waves. $k_{xj}=k_{xp}$ if $j=1$ and $k_{xj}=k_{xs}$ if $j=2, 3$. T_{mj}^- and T_{mj}^+ are expressed as

$$\begin{aligned}
T_{mj}^- &= \mathrm{i}^{-m}\begin{cases} \cos\left(m\beta_1\right),\ \beta_1 = \arcsin\left(k_y/k_{rp}\right),\ j=1 \\ \sin\left(m\beta_2\right),\ \beta_2 = \arcsin\left(k_y/k_{rs}\right),\ j=2 \\ \cos\left(m\beta_3\right),\ \beta_3 = \arcsin\left(k_y/k_{rs}\right),\ j=3 \end{cases} \\
T_{mj}^+ &= \mathrm{i}^{m}\begin{cases} \cos\left(m\beta_1\right),\ \beta_1 = \arcsin\left(k_y/k_{rp}\right),\ j=1 \\ -\sin\left(m\beta_2\right),\ \beta_2 = \arcsin\left(k_y/k_{rs}\right),\ j=2 \\ \cos\left(m\beta_3\right),\ \beta_3 = \arcsin\left(k_y/k_{rs}\right),\ j=3 \end{cases}
\end{aligned} \tag{S29}$$

Substituting Eqs. (S28) and (S29) into Eqs. (S17) and (S18) for layer n with a cavity, the displacement and traction vectors along its upper interface can be expressed in the following forms after some manipulations:

$$\begin{aligned}\hat{\hat{\tilde{\mathbf{u}}}}\left(x^n=H_{n1}\right)&=\hat{\hat{\tilde{\boldsymbol{\phi}}}}_a\left(x^n=H_{n1}\right)\mathbf{A}_a^n+\hat{\hat{\tilde{\boldsymbol{\phi}}}}_d\left(x^n=H_{n1}\right)\mathbf{A}_d^n+2\sum_{m=0}^{M}\hat{\hat{\tilde{\boldsymbol{\phi}}}}_a\left(x^n=H_{n1}\right)\mathbf{T}_m^-\mathbf{A}_o^m\\ \hat{\hat{\tilde{\boldsymbol{\sigma}}}}\left(x^n=H_{n1}\right)&=\hat{\hat{\tilde{\boldsymbol{\varphi}}}}_a\left(x^n=H_{n1}\right)\mathbf{A}_a^n+\hat{\hat{\tilde{\boldsymbol{\varphi}}}}_d\left(x^n=H_{n1}\right)\mathbf{A}_d^n+2\sum_{m=0}^{M}\hat{\hat{\tilde{\boldsymbol{\varphi}}}}_a\left(x^n=H_{n1}\right)\mathbf{T}_m^-\mathbf{A}_o^m\end{aligned}\tag{S30}$$

where $\mathbf{T}_m^-=\mathrm{diag}\left[\frac{T_{m1}^-}{k_{xp}}\quad\frac{T_{m2}^-}{k_{xs}}\quad\frac{T_{m3}^-}{k_{xs}}\right]$.

Analogously, displacement and traction vectors along the bottom interface can be expressed as

$$\begin{aligned}\hat{\hat{\tilde{\mathbf{u}}}}\left(x^n=-H_{n2}\right)&=\hat{\hat{\tilde{\boldsymbol{\phi}}}}_a\left(x^n=-H_{n2}\right)\mathbf{A}_a^n+\hat{\hat{\tilde{\boldsymbol{\phi}}}}_d\left(x^n=-H_{n2}\right)\mathbf{A}_d^n+2\sum_{m=0}^{M}\hat{\hat{\tilde{\boldsymbol{\phi}}}}_d\left(x^n=-H_{n2}\right)\mathbf{T}_m^+\mathbf{A}_o^m\\ \hat{\hat{\tilde{\boldsymbol{\sigma}}}}\left(x^n=-H_{n2}\right)&=\hat{\hat{\tilde{\boldsymbol{\varphi}}}}_a\left(x^n=-H_{n2}\right)\mathbf{A}_a^n+\hat{\hat{\tilde{\boldsymbol{\varphi}}}}_d\left(x^n=-H_{n2}\right)\mathbf{A}_d^n+2\sum_{m=0}^{M}\hat{\hat{\tilde{\boldsymbol{\varphi}}}}_d\left(x^n=-H_{n2}\right)\mathbf{T}_m^+\mathbf{A}_o^m\end{aligned}\tag{S31}$$

where $\mathbf{T}_m^+=\mathrm{diag}\left[\frac{T_{m1}^+}{k_{xp}}\quad\frac{T_{m2}^+}{k_{xs}}\quad\frac{T_{m3}^+}{k_{xs}}\right]$.

The compatibility and equilibrium conditions along the upper and bottom interfaces of the layer with a cavity with adjoining layers can be written as

$$\begin{aligned}&\hat{\hat{\tilde{\mathbf{u}}}}\left(x^{n-1}=0\right)=\hat{\hat{\tilde{\mathbf{u}}}}\left(x^n=H_{n1}\right),\ \hat{\hat{\tilde{\boldsymbol{\sigma}}}}\left(x^{n-1}=0\right)=\hat{\hat{\tilde{\boldsymbol{\sigma}}}}\left(x^n=H_{n1}\right),\ \text{upper interface}\\ &\hat{\hat{\tilde{\mathbf{u}}}}\left(x^{n+1}=0\right)=\hat{\hat{\tilde{\mathbf{u}}}}\left(x^n=-H_{n2}\right),\ \hat{\hat{\tilde{\boldsymbol{\sigma}}}}\left(x^{n+1}=0\right)=\hat{\hat{\tilde{\boldsymbol{\sigma}}}}\left(x^n=-H_{n2}\right),\ \text{bottom interface}\end{aligned}\tag{S32}$$

Considering Eqs. (S7), (S9), (S31), (S32), and the formulations in **Subsection 1.4**, the relationship between the unknown coefficient $\mathbf{A}^n$ for the plane waves and that $\mathbf{A}_o$=[$\mathbf{A}_o^1\ \mathbf{A}_o^2 \cdots \mathbf{A}_o^M]^{\mathrm{T}}_{(3(M+1)\times 1)}$ for the cylindrical waves for the layer with a cavity can be derived by only matrix manipulation. For simplicity, the relationship between $\mathbf{A}^n$ and $\mathbf{A}_o$ can be expressed as

$$\mathbf{A}^n=\begin{bmatrix}\mathbf{A}_a^n\\ \mathbf{A}_d^n\end{bmatrix}=\mathbf{T}_{(\mathbf{A}^n,\mathbf{A}_o)}\mathbf{A}_o=\begin{bmatrix}\mathbf{T}^a\\ \mathbf{T}^d\end{bmatrix}\mathbf{A}_o\tag{S33}$$

where $\mathbf{T}_{(\mathbf{A}^n,\mathbf{A}_o)}$ is a 6×3(M+1) coefficient matrix.

Furthermore, considering Eqs. (S24), (S32), and (S33), the relationship between $\mathbf{A}^1$ and $\mathbf{A}_o$ is obtained as follows:

$$\mathbf{A}^1=\mathbf{T}_{(\mathbf{A}^1,\mathbf{A}_o)}\mathbf{A}_o\tag{S34}$$

where $\mathbf{T}_{(\mathbf{A}^1,\mathbf{A}_o)}$ is a 6×3(M+1) coefficient matrix as well.

It can be observed that, if the unknown vector $\mathbf{A}_o$ is calculated, the unknown vector $\mathbf{A}^1$ for the first standard layer can be directly determined using Eq. (S34). Subsequently, by substituting $\mathbf{A}^1$ into Eq. (S19) yields the displacement responses of the ground surface induced by a dynamic load. The unknown vector $\mathbf{A}_o$ is determined from the coupling between the layer with a cavity and the hollow cylinder which suffers from the spatially periodic harmonic moving load at its inner interface.

1.6 Interaction between the layer with a cavity and hollow cylinder

To couple the layer with a cavity and hollow cylinder, the ascending and descending plane wave potentials should be expanded in terms of regular cylindrical wave potentials. The transformation properties have been proposed by Boström (1991) and can be written as

$$\hat{\tilde{\bar{\boldsymbol{\phi}}}}_{aj} \mathrm{e}^{\mathrm{i}k_y y} = \sum_{m=0}^{M} \varepsilon_m \tilde{\bar{\boldsymbol{\chi}}}_{rj}^{m} T_{mj}^{+}$$
$$\hat{\tilde{\bar{\boldsymbol{\phi}}}}_{dj} \mathrm{e}^{\mathrm{i}k_y y} = \sum_{m=0}^{M} \varepsilon_m \tilde{\bar{\boldsymbol{\chi}}}_{rj}^{m} T_{mj}^{-} \tag{S35}$$

where ε_m is the Neumann factor, ε_m=1 for m=0 and ε_m=2 for $m\geq 1$.

Substituting Eq. (S35) into Eqs. (S17) and (S18) for layer n with a cavity, the displacement and traction vector along the inner interface (r=R+h) of the cavity can be obtained after some manipulations as follows:

$$\tilde{\bar{\mathbf{u}}}_m^n(r=R+h) = \left[\frac{1}{2\pi}\int_{-\infty}^{+\infty} \varepsilon_m \tilde{\bar{\boldsymbol{\chi}}}_r^m(r=R+h)\left(\mathbf{T}_m^{+}\mathbf{T}^{a} + \mathbf{T}_m^{-}\mathbf{T}^{d}\right)\mathrm{d}ky + \tilde{\bar{\boldsymbol{\chi}}}_o^{m*}(r=R+h)\right]\mathbf{A}_o = \mathbf{C}_m^n(r=R+h)\mathbf{A}_o$$
$$\tilde{\bar{\boldsymbol{\sigma}}}_m^n(r=R+h) = \left[\frac{1}{2\pi}\int_{-\infty}^{+\infty} \varepsilon_m \tilde{\bar{\boldsymbol{\eta}}}_r^m(r=R+h)\left(\mathbf{T}_m^{+}\mathbf{T}^{a} + \mathbf{T}_m^{-}\mathbf{T}^{d}\right)\mathrm{d}ky + \tilde{\bar{\boldsymbol{\eta}}}_o^{m*}(r=R+h)\right]\mathbf{A}_o = \mathbf{D}_m^n(r=R+h)\mathbf{A}_o \tag{S36}$$

where $\mathbf{C}_m^n$ and $\mathbf{D}_m^n$ are 3×3(M+1) matrices. $\tilde{\bar{\boldsymbol{\chi}}}_r^m = \left[\tilde{\bar{\boldsymbol{\chi}}}_{r1}^m \quad \tilde{\bar{\boldsymbol{\chi}}}_{r2}^m \quad \tilde{\bar{\boldsymbol{\chi}}}_{r3}^m\right]$ and $\tilde{\bar{\boldsymbol{\eta}}}_r^m = \left[\tilde{\bar{\boldsymbol{\eta}}}_{r1}^m \quad \tilde{\bar{\boldsymbol{\eta}}}_{r2}^m \quad \tilde{\bar{\boldsymbol{\eta}}}_{r3}^m\right]$. $\tilde{\bar{\boldsymbol{\chi}}}_o^{m*}$ and $\tilde{\bar{\boldsymbol{\eta}}}_o^{m*}$ have the following expressions:

$$\tilde{\bar{\boldsymbol{\chi}}}_o^{m*} = \left[\mathbf{0}_{3\times 3} \quad \cdots \quad \tilde{\bar{\boldsymbol{\chi}}}_{o,\,3\times 3}^m \quad \cdots \quad \mathbf{0}_{3\times 3}\right]_{3\times 3(M+1)}$$
$$\tilde{\bar{\boldsymbol{\eta}}}_o^{m*} = \left[\mathbf{0}_{3\times 3} \quad \cdots \quad \tilde{\bar{\boldsymbol{\eta}}}_{o,\,3\times 3}^m \quad \cdots \quad \mathbf{0}_{3\times 3}\right]_{3\times 3(M+1)} \tag{S37}$$

Eq. (S36) can be calculated using the numerical quadrature technique. The state variable $\tilde{\bar{\mathbf{S}}}_m^n$ at the cavity interface can be defined as:

$$\tilde{\bar{\mathbf{S}}}_m^n = \begin{bmatrix} \tilde{\bar{\mathbf{u}}}_m^n(r=R+h) \\ \tilde{\bar{\boldsymbol{\sigma}}}_m^n(r=R+h) \end{bmatrix} = \begin{bmatrix} \mathbf{C}_m^n(r=R+h) \\ \mathbf{D}_m^n(r=R+h) \end{bmatrix}\mathbf{A}_o \tag{S38}$$

For a hollow cylinder, the state variable $\tilde{\bar{\mathbf{S}}}_m^{to}$ can be defined according to Eqs. (S11) and (S13), expressed as follows:

$$\tilde{\bar{\mathbf{S}}}_m^{to} = \begin{bmatrix} \tilde{\bar{\mathbf{u}}}_m^t(r=R+h) \\ \tilde{\bar{\boldsymbol{\sigma}}}_m^t(r=R+h) \end{bmatrix} = \begin{bmatrix} \tilde{\bar{\boldsymbol{\chi}}}_o^m(r=R+h) & \tilde{\bar{\boldsymbol{\chi}}}_r^m(r=R+h) \\ \tilde{\bar{\boldsymbol{\eta}}}_o^m(r=R+h) & \tilde{\bar{\boldsymbol{\eta}}}_r^m(r=R+h) \end{bmatrix}\mathbf{B}^m \tag{S39}$$

where $\mathbf{B}^m = \begin{bmatrix} \mathbf{B}_o^m \\ \mathbf{B}_r^m \end{bmatrix}$.

According to the compatibility and equilibrium conditions along the interface $\tilde{\bar{\mathbf{S}}}_m^n = \tilde{\bar{\mathbf{S}}}_m^{to}$, the following equation can be obtained

$$\mathbf{B}^m = \begin{bmatrix} \tilde{\bar{\boldsymbol{\chi}}}_o^m(r=R+h) & \tilde{\bar{\boldsymbol{\chi}}}_r^m(r=R+h) \\ \tilde{\bar{\boldsymbol{\eta}}}_o^m(r=R+h) & \tilde{\bar{\boldsymbol{\eta}}}_r^m(r=R+h) \end{bmatrix}^{-1}\begin{bmatrix} \mathbf{C}_m^n(r=R+h) \\ \mathbf{D}_m^n(r=R+h) \end{bmatrix}\mathbf{A}_o \tag{S40}$$

The unknown coefficients $\mathbf{B}^m$ for the tunnel structure and $\mathbf{A}_o$ for the layer with a cavity are related by Eq. (S40). Once $\mathbf{A}_o$ is known, $\mathbf{B}^m$ can be immediately calculated. Subsequently, the dynamic responses of the tunnel structure under the moving load can be determined using Eqs. (S11) and (S13).

S1.7 Moving load applied at the inner interface of the tunnel structure

The applied external load is periodic in space with a periodicity length L, harmonic in time with a circular frequency ω_l, and moves at a constant speed of v in the z-direction. The force applied at the inverted arch of the tunnel structure can be mathematically expressed as (Xu and Ma, 2022)

$$p\left(r,\varphi,z,t\right)=\frac{1}{R}\delta(r-R)\delta(\varphi-\pi)\delta\left(z-vt\right)\mathrm{e}^{\mathrm{i}\xi_n z}\mathrm{e}^{\mathrm{i}\omega_l t},\xi_n=\frac{2\pi n}{L} \tag{S41}$$

The origin of the moving load is located at (R, π, 0 m). By performing a Fourier transform with respect to t, the force in the frequency domain can be obtained as

$$\tilde{p}(r,\varphi,z,\omega)=\frac{1}{vR}\delta(r-R)\delta(\varphi-\pi)\mathrm{e}^{\mathrm{i}\lambda_n z} \tag{S42}$$

Considering the orthogonality of the generalised modal function, the components of the spatially periodic harmonic moving load can be expressed as follows:

$$\bar{\tilde{p}}_q(r,\varphi,\omega)=\begin{cases}\dfrac{1}{vR}\delta(r-R)\delta(\varphi-\pi), q=n\\ 0 \qquad\qquad\qquad\qquad\quad , q\neq n\end{cases} \tag{S43}$$

This means that only the n-th order components must be considered in the calculation of the spatially periodic harmonic load. Furthermore, the n-th order component should be expanded in terms of the trigonometric series, yielding

$$\bar{\tilde{p}}_n(r,\varphi,\omega)=\sum_{m=0}^{M}\bar{\tilde{p}}_m(r=R)=\sum_{m=0}^{M}\frac{\varepsilon_m}{2\pi vR}(-1)^m\delta(r-R)\cos m\varphi \tag{S44}$$

Therefore, the external load vector can be expressed as

$$\bar{\tilde{\mathbf{t}}}_m(r=R)=\left[\bar{\tilde{p}}_m(r=R)\quad 0\quad 0\right]^{\mathrm{T}} \tag{S45}$$

According to the stress boundary condition of the inner interface of the tunnel structure, the following formulation can be obtained:

$$\left[\bar{\tilde{\boldsymbol{\eta}}}_o^m(r=R)\quad \bar{\tilde{\boldsymbol{\eta}}}_r^m(r=R)\right]\mathbf{B}^m=\bar{\tilde{\mathbf{t}}}_m(r=R) \tag{S46}$$

Substituting Eq. (S40) into Eq. (S46) yields the following equation:

$$\left[\bar{\tilde{\boldsymbol{\eta}}}_o^m(r=R)\quad \bar{\tilde{\boldsymbol{\eta}}}_r^m(r=R)\right]\begin{bmatrix}\bar{\tilde{\boldsymbol{\chi}}}_o^m(r=R+h) & \bar{\tilde{\boldsymbol{\chi}}}_r^m(r=R+h)\\ \bar{\tilde{\boldsymbol{\eta}}}_o^m(r=R+h) & \bar{\tilde{\boldsymbol{\eta}}}_r^m(r=R+h)\end{bmatrix}^{-1}\begin{bmatrix}\mathbf{C}_m^n(r=R+h)\\ \mathbf{D}_m^n(r=R+h)\end{bmatrix}\mathbf{A}_o=\bar{\tilde{\mathbf{t}}}_m(r=R) \tag{S47}$$

This resulted in three equations for each m. After considering m=0, 1, 2, ⋯, M, there are 3(M+1) equations where there are 3(M+1) unknowns $\mathbf{A}_o$ as well. Therefore, the unknown coefficients $\mathbf{A}_o$ can be uniquely determined by solving Eq. (S47). Thereafter, the unknown coefficients for the tunnel structure $\mathbf{B}^m$ and first layer $\mathbf{A}^1$ can be derived based on Eqs. (S40) and (S34), respectively. Consequently, the dynamic response can be constructed by considering the corresponding formulations in **Subsection 1.3**. Notably, the formulations derived above were programmed in MATLAB, where M=12 was considered to obtain the convergence result. A rapid analysis of ground-borne vibrations from a tunnel under a spatially periodic harmonic moving load can be achieved using this program.

S2. Material parameters and additional cases in the validation

S2.1 Material parameters

To demonstrate the efficiency and accuracy of the proposed model, the ground-borne vibrations from the model in which the tunnel is embedded in a homogeneous and multilayered half-space were compared with those from the literature (He et al., 2018; Yuan et al., 2017). The material parameters involved were given below.

In the first case (Yuan et al., 2017), the soil in the half-space had a longitudinal wave velocity of c_p=146 m/s, a shear wave velocity of c_s=78 m/s, a material density of ρ=1900 kg/m^3, and hysteretic material damping ζ=0.05. The tunnel was made of concrete with a Young's modulus of E=25 GPa, Poisson's ratio v=0.2, material density ρ=2400 kg/m^3, and hysteretic material damping ζ=0.02. The inner radius and thickness of the tunnel structure were R=2.75 m and h=0.25 m, respectively. The distance between the axis of the tunnel and the ground surface was d=15 m.

In the second case (He et al., 2018), the multilayered half-space had three soil layers, the third of which was termed the half-space that extends to infinity. The first two layers had thicknesses of H=5 and 10 m, respectively. Soils in the half-space had shear velocities of v_s=50, 100, and 150 m/s, longitudinal velocities of v_p=100, 200, and 300 m/s, material density of ρ=1800 kg/m^3, and hysteretic material damping of ζ=0.04. The centre of the tunnel was buried at a depth of d=15 m and had an inner radius of R=2.75 m and a thickness of h=0.25 m. The Young's modulus of the tunnel concrete was E=50 GPa, Poisson's ratio v=0.3, material density ρ=2500 kg/m^3, and hysteretic material damping ζ=0.03.

S2.2 Additional comparisons

Additional comparisons of the calculated results with those from the analytical solution (Yuan et al., 2017) were given in the subsection.

Comparisons of vertical maximum velocities at the ground surface along the y-coordinate owing to the constant load f_0=0 Hz moving at the speed of v=10, 30, and 50 m/s with those from the analytical solution (Yuan et al., 2017) are shown in **Fig. S3**. Good agreements were observed from the results. The vertical maximum vibration attenuated along the y-coordinate under these circumstances.

Fig. S4 presents the comparison of the vertical and longitudinal displacements at (0 m, 0 m, 0 m) subjected to the harmonic load f_0=5 Hz moving at the speed of v=30 m/s with those from the analytical solution (Yuan et al., 2017). Again, results from the current model agreed well with those from the reference. At the time instant t=0 s when the load moved to the position beneath the observation point, the vertical displacement reached the maximum while the longitudinal one reached the minimum.

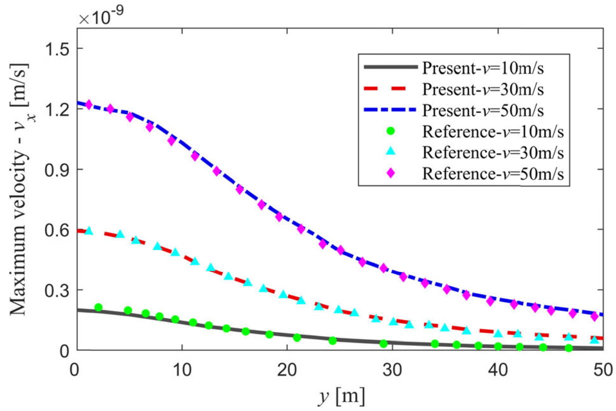

Fig. S3 Comparison of vertical maximum velocity along the y-axis at the ground under the constant load (f_0=0 Hz) moving at the speed of 10, 30, and 50 m/s.

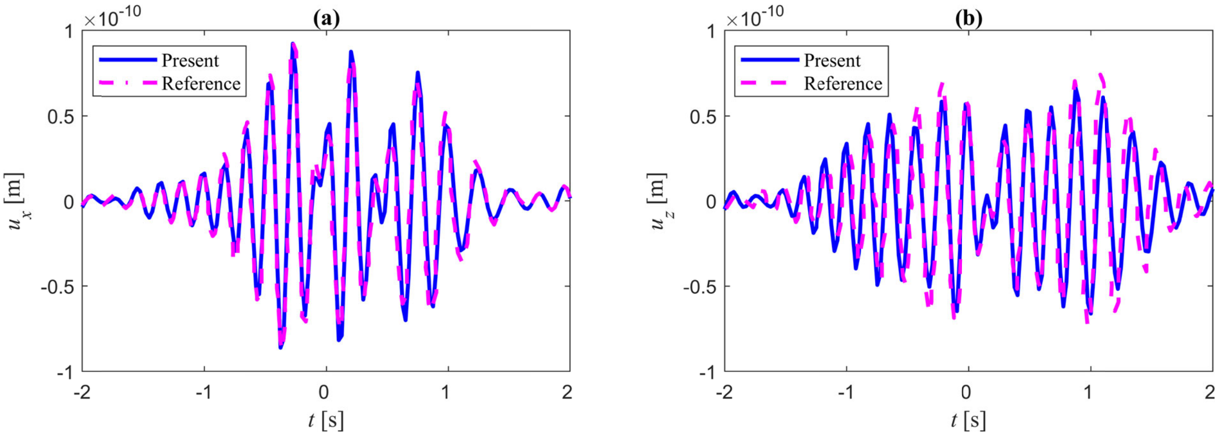

Fig. S4 Comparison of (a) vertical and (b) longitudinal displacement history u_x and u_z at (0 m, 0 m, 0 m) under moving harmonic load (v=30 m/s, f_0=5 Hz).

S3. Additional numerical results

S3.1 General velocity results

Fig. S5 shows the corresponding velocity responses at points A (0 m, 0 m, 0 m) and B (0 m, 10 m, 0 m) on the ground surface in both the time and frequency domains, from which the observations from displacements in **Fig. S7 in the main manuscript** can also be noticed. Notably, the velocity vibrations were much stronger than the displacement vibrations. This is because the velocity $\tilde{\mathbf{v}}$ in frequency domain can be deduced from the displacement $\tilde{\mathbf{u}}$ in frequency domain, obeying the relation $\tilde{\mathbf{v}} = \mathrm{i}2\pi f\tilde{\mathbf{u}}$, and the frequency f spreads around the critical frequency f_{cr}.

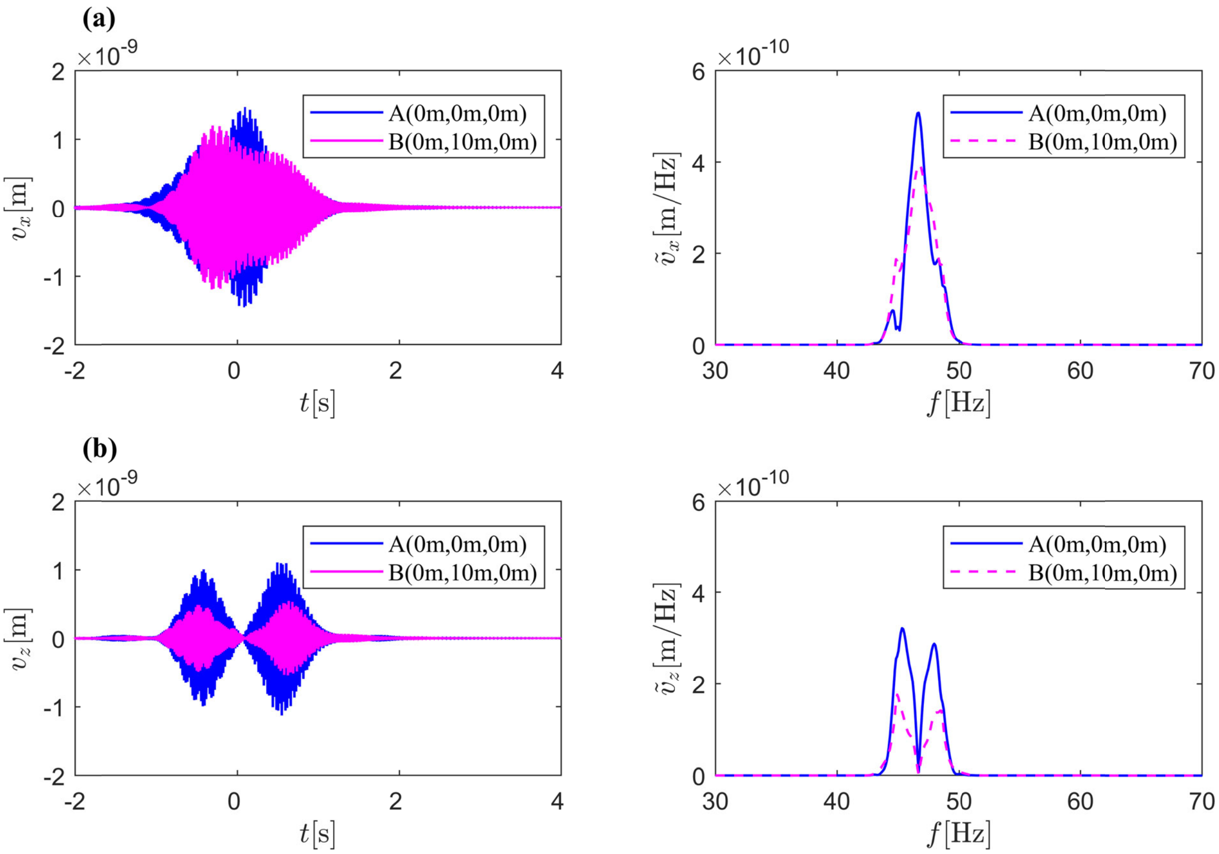

Fig. S5 (a) Vertical velocity v_x and (b) longitudinal velocity v_z in time and frequency domain at A (0 m, 0 m, 0 m) and B (0 m, 10 m, 0 m) of the ground surface.

S3.2 Maximum and instantaneous displacements along the *y*-axis

The maximum and instantaneous displacements at t=0 s along the y-axis under a spatially periodic harmonic moving load are presented in **Fig. S6**. Unlike the ground vibration which is consistently weakened by the soil along the y-axis under a moving constant load (Yuan et al., 2017), the vibration under the spatially periodic harmonic moving load shows undulating behaviours similar to those under a harmonic moving load, as shown in **Fig. S6**a. The highest vertical vibration level along the ground surface appears at a point with a lateral distance of approximately 18 m owing to the propagating waves emanating from the tunnel. The longitudinal vibration is generally weaker and attenuates more quickly than the vertical vibration, which can also be observed **in Fig. S6**b. The wavelengths of the vertical and longitudinal displacements were almost the same, and the propagating waves were excited, even under a load velocity of v=25 m/s.

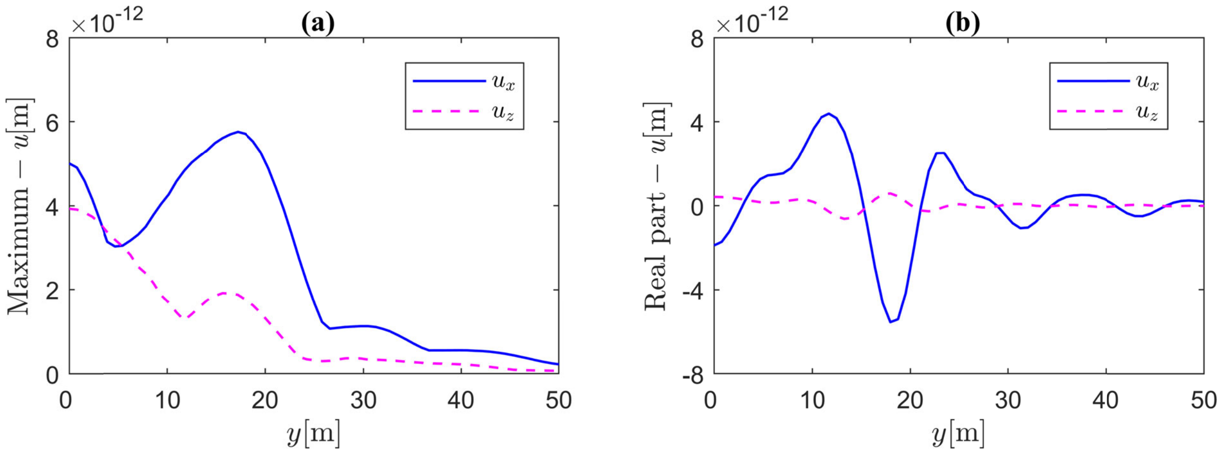

Fig. S6 (a) maximum displacement and (b) instantaneous displacement at the time instant t=0 s on the ground surface in both vertical and longitudinal direction along the y-axis.

S3.3 Instantaneous displacements and velocities along the *z*-axis

Fig. S7 shows the instantaneous displacements and velocities at the time instant t=0 s along the z-axis under a spatially periodic harmonic load. It can be observed that the vibrations mainly exist within a certain area and decay quickly along the z-axis. Clearly, the vertical displacement and velocity at t=0 s are not perfectly symmetric with respect to z=0, whereas the longitudinal displacement and velocity at t=0 s are not perfectly antisymmetric owing to the Doppler effect. The velocity responses were much stronger than the displacement responses, and similar observations were found by Yuan et al. (2017). In some areas, longitudinal vibrations are stronger than vertical vibrations. The wavelengths of the vertical and longitudinal vibrations were almost the same, and propagating waves could be observed. Comparing the results from **Fig. S7**a and **Fig. S6**b, wavelengths along the z-axis are larger than those along the y-axis, which is because the waves in the tunnel structure travel much faster than those in the soil.

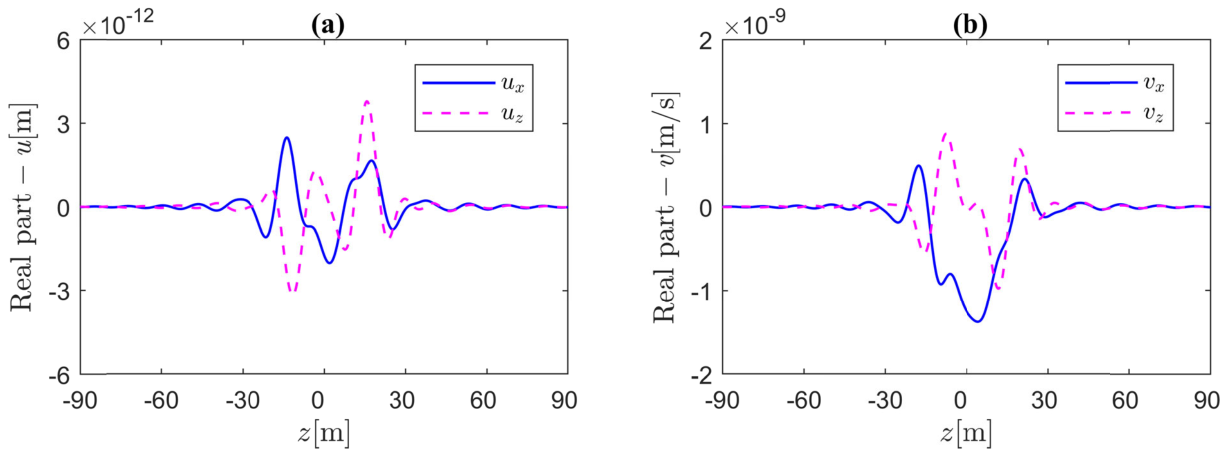

Fig. S7 Instantaneous (a) displacement and (b) velocity at the time instant t=0 s on the ground surface in both vertical and longitudinal direction along the z-axis.

Reference

Belotserkovskiy PM, 1996. On the oscillations of infinite periodic beams subjected to a moving concentrated force. *J Sound Vib* 193(3): 705-712.

Belotserkovskiy PM, 1998. Forced oscillations of infinite periodic structures. Applications to railway track dynamics. *Vehicle Syst Dyn* 29(1): 85-103.

Boström A, Kristensson G, Ström S, 1991. Transformation properties of plane, spherical, and cylindrical scalar and vector wave functions. In: field representations and introduction to scattering. Amsterdam: Elsevier, pp. 165-210.

Haskell NA, 1953. The dispersion of surface waves on multi-layered media. *B Seismol Soc Am* 43: 17-34.

He C, Zhou S, Di H, et al., 2018. Analytical method for calculation of ground vibration from a tunnel embedded in a multi-layered half-space. *Comput Geotech* 99: 149-164.

He C, Zhou S, Guo P, et al., 2017. Dynamic 2.5D green's function for a point load or a point fluid source in a layered poroelastic half-space. *Eng Anal Bound Elem* 77: 123-137.

Hussein MFM, Hunt HEM, 2009. A numerical model for calculating vibration due to a harmonic moving load on a floating-slab track with discontinuous slabs in an underground railway tunnel. *J Sound Vib* 321(1-2): 363-374.

Kausel E, 2006. Fundamental solutions in elastodynamics- a compendium. Cambridge University Press, New York.

Ma L, Liu W, 2018. A numerical train − floating slab track coupling model based on the periodic-Fourier-modal method. *P I Mech Eng F-J Rai* 232(1): 315-334.

Pilant WL, 1979. Elastic waves in the earth. Elsevier Scientific Publishing Company, New York.

Schevenels M, 2007. The impact of uncertain dynamic soil characteristics on the prediction of ground vibrations. Catholic University of Leuven, Leuven.

Sheng X, Jones C J C, Thompson D J. Moving Green's functions for a layered circular cylinder of infinite length. Southampton: ISVR Technical Memorandum No. 885, 2002.

Thomson WT, 1950. Transmission of elastic waves through a stratified solid medium. *J Appl Phys* 21(2): 89-93.

Xu, L., Ma, M., 2022. Dynamic response of the multilayered half-space medium due to the spatially periodic harmonic moving load. *Soil Dyn Earthq Eng* 157: 107246.

Yuan Z, Boström A, Cai Y, 2017. Benchmark solution for vibrations from a moving point source in a tunnel embedded in a half-space. *J Sound Vib* 387: 177-193.